Three-Dimensional Reverse-Time Migration Applied to a MIMO GPR System for Subsurface Imaging

H. Liu, Y. X. Zhang, Z. J. Long, F. Han
Institute of Electromagnetics and Acoustics, and Department of Electronic Science, Xiamen University, Xiamen, 361005, China.
liuhai8619@xmu.edu.cn, yxzhang@stu.xmu.edu.cn

Q. H. Liu
Department of Electrical and Computer Engineering, Duke University, Durham, NC 27708, USA
qhliu@duke.edu

***Abstract*—Compared with a conventional single-channel GPR system, a GPR system with a multi-input and multi-output (MIMO) antenna array is not only more efficient in 3D data acquisition, but also allows the collection of a multi-offset dataset, thereby providing additional information for more effective subsurface imaging. We develop a three-dimensional (3-D) reverse time migration (RTM) algorithm for processing MIMO GPR data. The finite-difference time-domain method with a convolutional perfect matching layer boundary is used to simulate the propagation of electromagnetic waves in subsurface dissipative media. The range and lateral resolution of a MIMO GPR system, which works at a stationary mode, is analyzed by numerical experiments. Furthermore, results of laboratory experiments would be presented in the extended abstract.**

***Index Terms*—GPR system, reverse time migration (RTM), finite-difference time-domain method.**

I. Introduction

Ground penetrating radar (GPR) has been popularly applied in various fields [1]–[4] to implement non-destructive detection and imaging. With a pair of antennas, a GPR system moves along a survey line transmitting and receiving electromagnetic waves, and then acquires dense discrete data. Generally, a synthetic aperture radar (SAR) algorithm is used to process common-offset GPR data and to improve the lateral imaging resolution [4][5][7]. Compared with the conventional single-channel GPR system, a GPR system with a multi-input and multi-output (MIMO) antenna array shows more efficiency in 3D data acquisition and allows the collection of multi-offset dataset. Thereby, additional information can be provided for more effective subsurface imaging and detection [8].

In 2017, a MIMO GPR system will be launched to the moon by the Chinese Chang-E 5 lunar exploration mission. Equipped with twelve off-ground Vivaldi antennas, one of these antennas is sequentially applied as a transmitter and the other eleven receive the radar echoes at a height of about 90 cm above the ground surface. However, unlike a normal GPR system, this MIMO GPR system works in a stationary mode. We have to image the lunar regolith structure and estimate the dielectric properties of the lunar soil and rock from the total of 132 radar echoes.

We have developed a reverse-time-migration (RTM) algorithm to obtain a high-resolution image of lunar regolith structures. The principle is presented in the second section and the results of both the experiments in two-dimensional (2-D) and three-dimensional (3-D) cases are respectively shown in the third and the fourth sections. In the fifth section, based on the data from laboratory experimentation, underground objects can be found after applying the RTM code simulation. The conclusion will be given in the last section.

II. RTM Algorithm

Recently, the RTM algorithm was developed as a novel algorithm for imaging geological structures in seismic exploration. We apply it to the processing of MIMO GPR datasets and the principle of a 2-D RTM algorithm is briefly given by:

$$I(x,z) = \sum_m \sum_n T_m(n\Delta t, x, z) R_m(n\Delta t, x, z) \quad (1)$$

where $T_m(n\Delta t, x, z)$ is the electromagnetic field distribution radiated from the m-th transmiting antenna at the n-th time step, $R_m(n\Delta t, z, x)$ presents the back-propagated field from the recorded field by the eleven receiving antennas, and $I(x, z)$ is the RTM image in a 2-D case with the x- and z-axis. The superscript m is the number of the transmitting antenna and n is the number of time steps. For 3-D cases, Equation (1) can be written as:

$$I(x,y,z) = \sum_m \sum_n T_m(n\Delta t, x, y, z) R_m(n\Delta t, x, y, z) \quad (2)$$

where $I(x, y, z)$ is the RTM image in 3-D cases. Equations 1 and 2 reflect the cross-correlation process as the imaging condition. The finite-difference time-domain (FDTD) method with the conventional perfectly matched layer can be applied to solve the Maxwell's equations and calculate the electromagnetic fields for implementing the

978-1-5090-5181-6/16/$31.00 @2016 IEEE

RTM results. The time-domain iterative formula can be written as:

$$\boldsymbol{H}^{n+1|2} = C_{HH}\boldsymbol{H}^{n-1|2} + C_{HE}(\partial \boldsymbol{E}^{n}) \quad (3)$$

$$\boldsymbol{E}^{n+1} = C_{EE}\boldsymbol{E}^{n} + C_{EH}(\partial \boldsymbol{H}^{n+1|2}) + \boldsymbol{J}^{n+1|2} \quad (4)$$

where n is the number of the time steps; $\boldsymbol{E}$, $\boldsymbol{H}$ and $\boldsymbol{J}$ represent the electric fields, magnetic fields, and current source of the antennas, which have three components corresponding with the x-, y- and z-axes; and $\partial\boldsymbol{E}$ and $\partial\boldsymbol{H}$ are the curl variation of $\boldsymbol{E}$ and $\boldsymbol{H}$ in the space. The C_{HH}, C_{HE}, C_{EE}, and C_{EH} are the iterative constants for the FDTD method. If the E_y component needs to be considered for the RTM simulation, then Equation (2) can be applied and $I_{Ey}(x, y, z)$ can be computed to see the imaging results.

III. 2-D Numerical Experiment

Only ten antennas are applied in the 2-D RTM algorithm since two of the twelve antennas are out of the imaging plane. For these antennas, the layout is shown in Fig. 1. This section shows the results of numerical experiments and a laboratory test. An initial model required by the FDTD simulation in the RTM is shown in Fig. 1. The relative dielectric permittivity and electric conductivity of the lunar soil are respectively set to be 2.5 and 0.01 mS/m. Since no prior information about the regolith structure and the buried objects could be obtained, a half-space initial model is employed for the 2D RTM. The problems under the lunar soil are unknown. After the RTM processing, we can forecast the shape of the object.

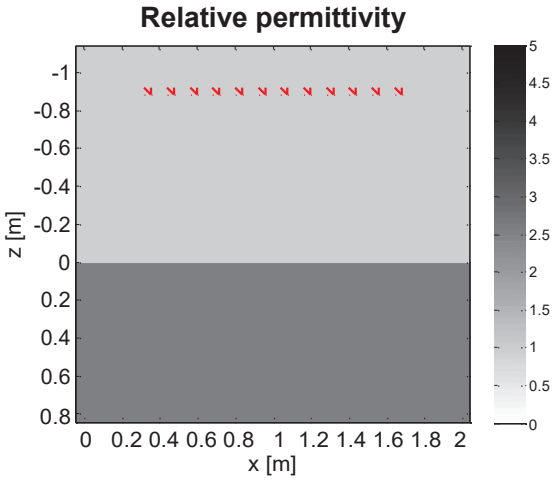

Fig. 1. Initial model used for the 2-D RTM. The colorbar indicates the dielectric permittivity and the cross symbolsdenote the positions of the ten antennas.

As shown in Fig. 2, the 2-D model of a numerical experiment is depicted. Two 5 cm diameter cylindrical rocks are buried at a depth of 50 cm in the lunar soil. Ten FDTD simulations are run to produce the MIMO GPR dataset. From the simulated dataset, the RTM image is shown in Fig. 3. The antennas' positions can be seen in the bright points. The interface between the air and lunar soil has been separated by a straight line. Two objects can be clearly identified. The basic outline forms two circles like the original objects in the lunar soil.

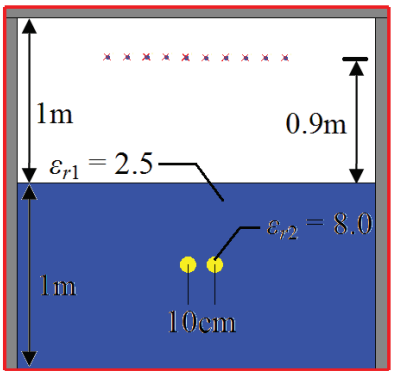

Fig. 2. Geometry of a 2-D simulation model. The colorbar indicates the dielectric permittivity and the cross symbols denote the positions of the ten antennas.

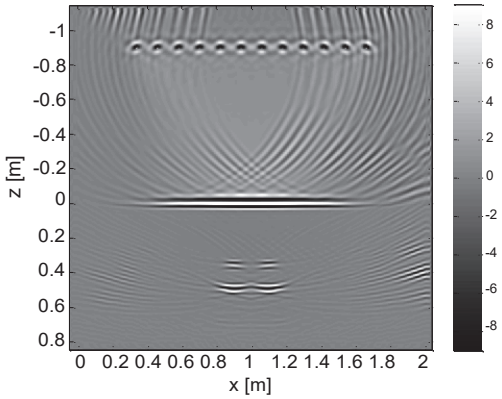

Fig. 3. The 2-D RTM image of the numerical dataset

IV. 3-D Numerical Experiment

The RTM algorithm in 3-D cases has a greater significance to the display of the three-dimensional structure. The resolution needs to be discussed carefully. For simulation cases, as in the MIMO GPR system, 16 antennas are chosen as the transverse arrangement along the y-axis. The permutations of the known object are considered and simulated. As shown in Fig. 5, the whole computational region is 2m × 2m × 2m and is air.

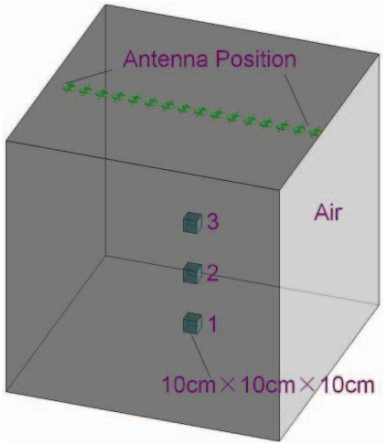

Fig. 5. Geometry of a 3-D simulation model. The entire region indicates the air and the green circle symbol denotes the positions of the 16 antennas. The 3 objects are on the same vertical line for xy plane and have the same volume 10cm × 10cm × 10cm.

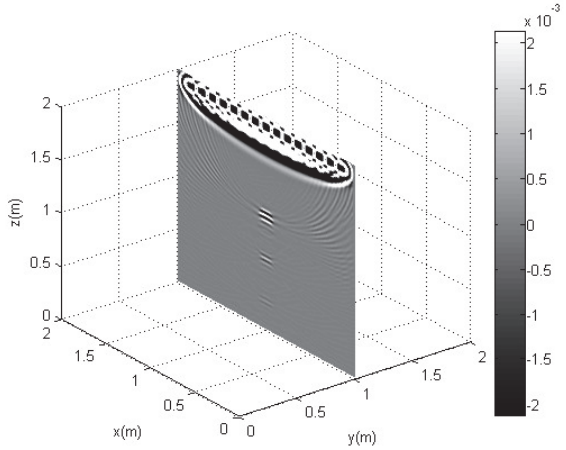

Fig. 6. The 3-D RTM image of the numerical dataset in *zx* plane.

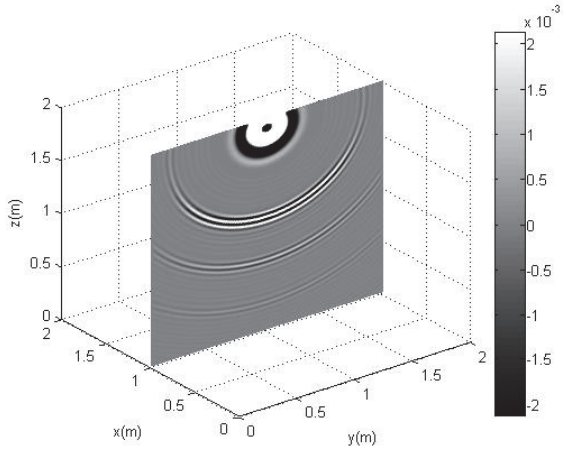

Fig. 7. The 3-D RTM image of the numerical dataset in *yz* plane.

The three objects are vertically arranged under the 16 antennas. The relative dielectric permittivity and electric conductivity of these objects are respectively set to be 1.0 and 10^5 S/m. After the RTM simulation, object No.1, No.2, and No.3 can be separated at different depths from Fig. 6 and Fig. 7. As the antenna position is based on a linear distribution, the three objects' images show a good performance along the antenna position, and these are shown in Fig. 8(a) – (c).

V. Laboratory Experiment

The Chinese Chang-E 5 lunar exploration mission is in preparation. In the laboratory, volcanic ash is selected as the experimental material because its electromagnetic properties are close to those of lunar soil. The MIMO GPR system is located above the ground to detect an unknown object. A marble slab is buried at 2.0m depth in the volcanic ash pit, as shown in Fig. 9. At the depth of 2.5 m, there is a metal plate in the bottom of the ash pit. The relative dielectric permittivity of volcanic ash is about 2.5, and its electrical conductivity is negligibly small. The thickness and relative dielectric permittivity of the marble slab are 3 cm and about 8, respectively. After running the experiment, we can record a total of 132 radar echoes and the transmitting signal from the MIMO GPR system.

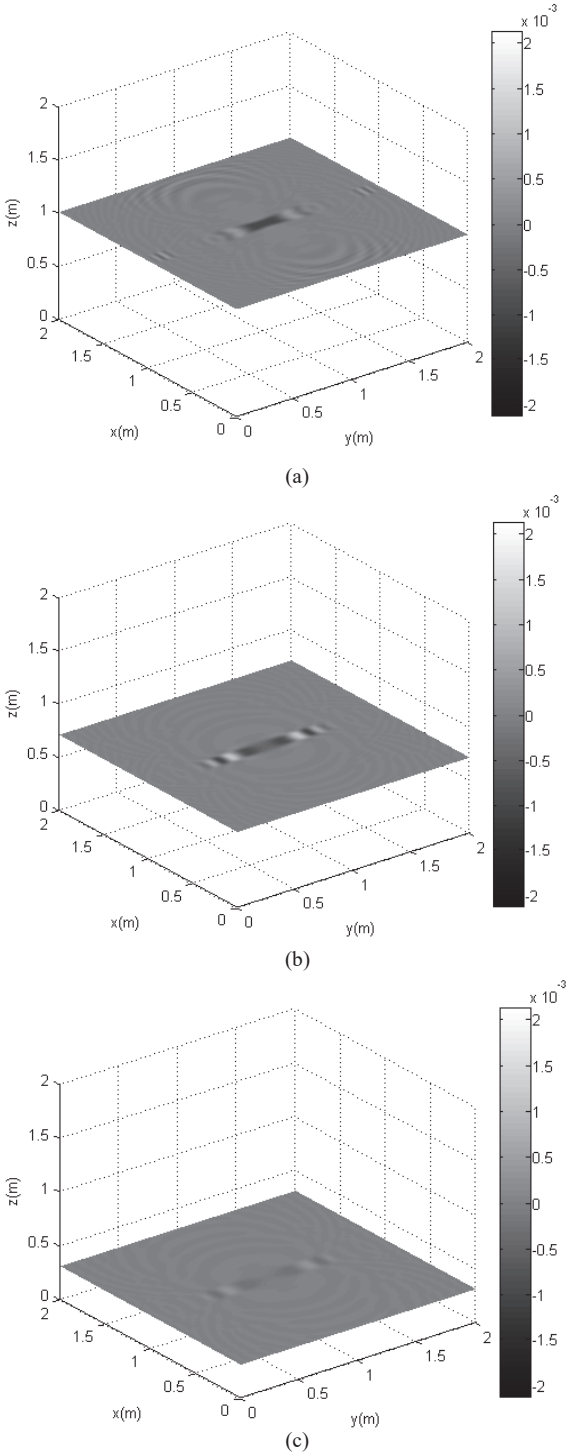

Fig. 8. The 3-D RTM image of the numerical dataset in *xy* plane at: (a) z = 1.0m; (b) z = 0.7m; (c) z = 0.3m.

Using the experimental data, the RTM code can be executed to search for the marble slab. Imaging results are successfully obtained at 2.0m depth as shown in Fig. 10. Although the

marble slab is only 3 cm in thickness, we can identify the upper and lower interfaces of this structure. It can be seen that the MIMO GPR system has a depth resolution better than 3 cm in marble rock. Considering the velocity difference in marble and lunar soil, it is concluded that the MIMO GPR system has a depth resolution of about 5 cm in the lunar soil. Furthermore, we repeated similar experiments when two marble slabs were buried at depths of 1.0 m and 1.5 m in the shallow zone. Without the jamming from the bottom of the ash pit, both of them will show better imaging results than in Fig. 10.

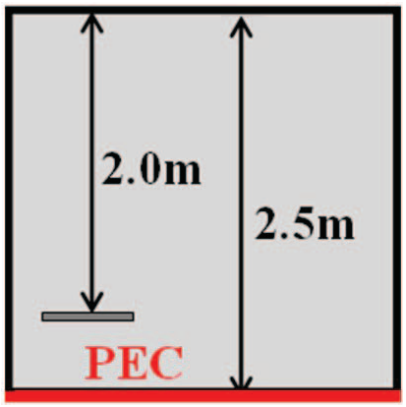

Fig. 9 Schematic diagram of the laboratory test.

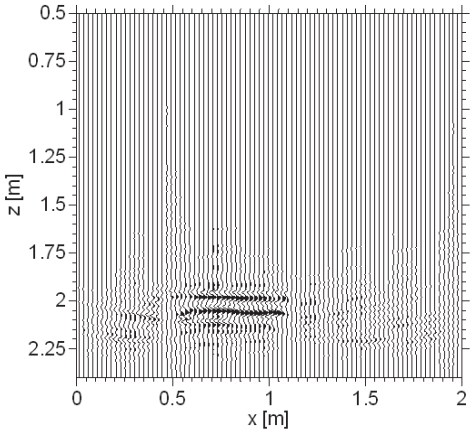

Fig. 10. The 3D-RTM results of the laboratory experiment in the 2.0m depth.

VI. Conclusion

In this paper, a stationary MIMO GPR system for shallow lunar exploration was introduced. To obtain a high-resolution subsurface image from the MIMO GPR dataset, a RTM algorithm was developed and verified by both numerical and laboratory experiments in 2-D and 3-D cases. The horizontal resolution was about 10 cm at a 50 cm depth and increased with depth. The depth resolution was verified to be less than 5 cm in lunar soil and 3 cm in lunar rock. A numerical experiment demonstrated that the dielectric permittivity of both the lunar soil and target rock can be accurately estimated from the MIMO GPR dataset at only six discrete frequencies.

Acknowledgment

This work was supported by National Natural Science Foundation of China (No. 41504111) and the Fundamental Research Funds for the Central Universities, Xiamen University (No. 20720150083). We are grateful to the group of Prof. Guangyou Fang in the Key Laboratory of Electromagnetic Radiation and Sensing Technology, CAS, China for providing the experimental dataset.

References

[1] H. Liu and M. Sato, “In situ measurement of pavement thickness and dielectric permittivity by GPR using an antenna array,” NDT E Int., no. 64, pp. 65–71, Jun 2014.

[2] H. Liu, K. Takahashi, and M. Sato, “Measurement of Dielectric Permittivity and Thickness of Snow and Ice on a Brackish Lagoon Using GPR,” IEEE J. Sel. Top. Appl. Earth Obs. Remote Sens., vol. 7, no. 3, pp. 820–827, Mar 2014.

[3] H. Liu, X. Xie, J. Cui, K. Takahashi, and M. Sato, “Groundwater Level Monitoring for Hydraulic Characterization of an Unconfined Aquifer by Common Mid-point Measurements using GPR,” J. Environ. Eng. Geophys., vol. 19, no. 4, pp. 259–268, 2014.

[4] L. Xiao, P. Zhu, G. Fang, Z. Xiao, Y. Zou, J. Zhao, Y. Yuan, L. Qiao, X. Zhang, H. Zhang, J. Wang, J. Huang, Q. Huang, Q. He, B. Zhou, Y. Ji, Q. Zhang, S. Shen, Y. Li, and Y. Gao, “A young multilayered terrane of the northern Mare Imbrium revealed by Chang’E-3 mission,” Science (80-.)., vol. 347, no. 6227, pp. 1226–1230, 2015.

[5] J. I. Halman, K. A. Shubert, and G. T. Ruck, “SAR processing of ground-penetrating radar data for buried UXO detection: results from a surface-based system,” IEEE Trans. Antennas Propag., vol. 46, no. 7, pp. 1023 –1027, 1998.

[6] K. Gu, G. Wang, and J. Li, “Migration based SAR imaging for ground penetrating radar systems,” Radar, Sonar Navig. IEE Proc. -, vol. 151, no. 5, pp. 317 – 325, Oct 2004.

[7] X. Feng, Y. Yu, C. Liu, and M. Fehler, “Combination of H-Alpha Decomposition and Migration for Enhancing Subsurface Target Classification of GPR,” IEEE Trans. Geosci. Remote Sens., vol. 53, no. 9, pp. 4852–4861, 2015.

[8] Z. Zeng, J. Li, L. Huang, X. Feng, and F. Liu, “Improving target detection accuracy based on multipolarization MIMO GPR,” IEEE Trans. Geosci. Remote Sens., vol. 53, no. 1, pp. 15–24, 2015.

[9] C. Yu, S. Member, M. Yuan, Y. Zhang, J. Stang, R. T. George, G. A. Ybarra, W. T. Joines, and Q. H. Liu, “Microwave Imaging in Layered Media : 3-D Image Reconstruction From Experimental Data,” IEEE Trans. Antennas Propag., vol. 58, no. 2, pp. 440–448, 2010.

[10] X. Millard, Q. H. Liu, and S. Member, “Simulation of Near-Surface Detection of Objects in Layered Media by the BCGS – FFT Method,” IEEE Trans. Geosci. Remote Sens., vol. 42, no. 2, pp. 327–334, 2004.